Hindawi
International Journal of Energy Research
Volume 2023, Article ID 5568642, 19 pages
https://doi.org/10.1155/2023/5568642

Research Article

Analysis of Thermal Runaway in Pouch-Type Lithium-Ion Batteries Using Particle Image Velocimetry

Donghwan Kim,[1] Inhan Sim,[1] Jisoo Shin,[1] and Sungwook Park[2]

[1]*Department of Mechanical Convergence Engineering, Graduate School of Hanyang University, Seoul 04763, Republic of Korea*
[2]*School of Mechanical Engineering, Hanyang University, Seoul 04763, Republic of Korea*

Correspondence should be addressed to Sungwook Park; parks@hanyang.ac.kr

Received 28 August 2023; Revised 3 November 2023; Accepted 13 November 2023; Published 30 November 2023

Academic Editor: Ahmad Azmin Mohamad

Copyright © 2023 Donghwan Kim et al. This is an open access article distributed under the Creative Commons Attribution License, which permits unrestricted use, distribution, and reproduction in any medium, provided the original work is properly cited.

Despite widespread recognition of the serious risk of battery thermal runaway (BTR) in lithium-ion batteries, the process and associated external ignition mechanism remain poorly understood. In this study, BTR was measured using thermodynamics and visualization techniques in 10 lithium-ion batteries under thermal abuse conditions. The venting speed was measured by particle image velocimetry and boundary detection. The external ignition mechanism was characterized in terms of flame area. The average BTR onset temperature across the 10 test batteries was 215.6°C. The average maximum temperature was 831.1°C, and the variation between experiments was high compared with the BTR onset temperature due to swelling, repairing, and venting. BTR occurred in four stages (ejection of vent gas with flame, extinction of flame, random and simultaneous ignition, and flame propagation and flame jet formation). The initial average venting speed was approximately 123.8 m/s. The structural and venting speeds of vent gas were similar after a stable flame jet formed. The speed of the core of the gas jet peaked at 20 to 40 m/s. The venting speed decreased as the distance from the jet core increased.

1. Introduction

Unprecedented climate change due to rising anthropogenic carbon emissions since the onset of the Industrial Revolution is a well-documented phenomenon, and efforts are being made to reduce carbon dioxide emissions worldwide [1]. To reduce emissions from the transportation sector, which accounts for 20% of industry-related carbon emissions, governments and companies around the world are attempting to replace internal combustion engines with electric battery-powered vehicles [2–4]. However, as reported previously, several problems with electric vehicles remain to be solved. First, from a life cycle perspective, electric vehicles still generate carbon dioxide emissions [5]. The energy density of batteries also tends to be lower than that of the fossil fuels used to power an internal combustion engine, hindering long-distance driving. Much research is now devoted to reducing battery charging times and lowering costs [6–8]. In addition, electric vehicle charging stations must have constant access to electricity, and active government support is required to build and maintain the charging infrastructure. Lithium-ion batteries with a high-energy density and long cycle life [9–11] are currently considered the most reasonable choice for electric vehicle batteries [12, 13]. However, the most concerning issue is battery safety, especially the risk of battery thermal runaway (BTR). Numerous cases of battery-related accidents have been reported over the past decade [14, 15], with BTR-induced smoke, fires, and explosions the most commonly reported accidents involving lithium-ion batteries. BTR has various causes and is difficult to control or suppress. To successfully expand the supply of electric vehicles, it is necessary to fully understand BTR and to find ways to mitigate it [16, 17]. BTR has been reported to be caused by mechanical abuse, electrical abuse, and thermal abuse. In mechanical abuse, the battery separator is torn by collision or crushing during a car accident, and BTR occurs due to an internal short circuit [18]. Additionally, combustible electrolyte may accidentally leak to the outside and be ignited by an external ignition source, resulting in BTR. Penetration is another common

phenomenon during a car crash and can cause internal short circuit quickly [19, 20]. The external short circuit [21, 22], overcharge [22–24], and overdischarge [25–27] are common causes of BTR due to the electrical abuse. Overheating caused by poor connection or high-temperature environment can also cause BTR [14, 28, 29]. A characteristic of BTR is that it is mostly accompanied by an internal short circuit. When an internal short circuit occurs, the separator is damaged and the anode and cathode come into contact, releasing high-temperature heat through a rapid oxidation-reduction reaction. In addition to causes such as external shocks, spontaneous internal short circuits caused by contamination or defects during manufacturing can also occur [30]. These chemical reactions produce combustible gases and, together with electrolyte vapor and continuously generated energetic substances, increase the pressure inside the battery cell, which can cause damage [31, 32]. Gas generation is affected by external conditions, state of charge (SOC), and battery aging state. In most experimental studies, venting process occurred before the BTR, independent of battery chemistry and SOC. The sequence of physical and chemical processes in BTR has been examined in various studies. The discharged combustible gas can ignite inside or outside the battery depending on conditions such as temperature, pressure, speed, electrolyte composition, and external convection. Combustible gases can ignite due to causes such as sparks, hot particles, or spontaneous combustion, but the flame can be extinguished depending on the flame propagation speed and oxygen concentration. As a result, in the case of a serious battery fire, the requirements for both ignition event and flame propagation must be met. Studies on various ignition mechanisms represent the need for in-depth understanding and analysis of vent gas ignition and combustion. Gas composition and solid particle composition are major factors affecting combustion reactions and have been investigated through experimental approaches [33–37]. Additionally, ignition characteristics, flame propagation speed, contaminant formation, laminar combustion speed, heat release rate, etc. have been studied using computational fluid dynamics to understand BTR [38–40].

Direct observation of a phenomenon is an intuitive and effective method. Optical diagnostics have been commonly used to visualize fuel spray and combustion in the field of combustion engine [41–43]. In BTR, the released combustible gas and electrolyte are ignited by an ignition source or high temperature, and the flame propagates. This process is similar to an internal combustion engine in terms of combustion characteristics. Therefore, optical diagnostics have been used to analyze the combustion of BTR.

Jia et al. [44] utilized visualization results to evaluate BTR characteristics at the low-pressure conditions. Fang et al. [45] analyzed BTR characteristics depending on SOC and spacing based on the temperature data with visualization results. Thermal runaway suppression effect of water mist was also evaluated using visualization [46–48]. However, they did not observe BTR by applying special optical techniques and used it for qualitative analysis. On the other hand, some researchers actively used visualization techniques in BTR analysis to quantitatively measure flame structure, gas composition, and gas velocity. Chen et al. [49] used infrared imaging technique to observe the outlines of a jet fire and high-temperature mixture in BTR. Tschirschwitz et al. [50] investigated vent gas composition qualitatively by using Fourier transform infrared and diode laser spectroscopy. Finegan et al. [51] used high-speed synchrotron X-ray computed tomography and radiography with thermal imaging. They evaluated internal structural damage and thermal behaviour during BTR. Visualization results can be also utilized to validate simulation model. Wang et al. [52] used laser tomography to validate multiscale model for battery venting. Recently, BTR visualization was performed by applying schlieren and natural luminosity techniques in a constant volume chamber which is used to visualize fuel spray, as reported by García et al. [53–55]. They confirmed the BTR generation temperature based on temperature data and visualization data. They characterized the liquid electrolyte, venting gas, and combustion processes using a high-speed camera. Additionally, the BTR process according to ambient air composition and SOC was quantified by measuring venting speed and venting angle. However, the small volume of the chamber resulted in low image quality, which limited quantitative analysis.

Table 1: The sequence of battery charging.

Step	Action	Mode	Control parameter	Value
1	Rest	Soaking	Temperature	25°C
			Time	1 h
2	Discharge	Constant current	Current	1/3 C
			Voltage limit	2.5 V
3	Rest		Time	20 min
4	Charge	Constant current	Current	1/3 C
			Voltage limit	4.2 V
		Constant voltage	Voltage	4.2 V
			Current limit	1/20 C
5	Rest		Time	1 h

Despite various BTR evaluations and interpretations, quantitative characterization of the flame propagation process and ignition mechanism remain insufficient. In addition, most previous studies which conducted visualization of BTR process adopted low frame rate and wide visualized areas, making it difficult to analyze the flame propagation process and initial ignition. In this study, BTR onset temperature and maximum temperature were measured in 10 lithium nickel cobalt manganese oxide (NCM) 811 batteries. We quantified BTR by calculating venting speed using particle image velocimetry (PIV) and a boundary detection method. Four stages of external ignition mechanism are explored, and the characteristics of each stage are described using calculations of flame area. These quantitative analyses and indices can be used to establish simulation models and validation.

2. Methodology

This section provides information on lithium-ion cells and experimental conditions for visualizing BTR during thermal

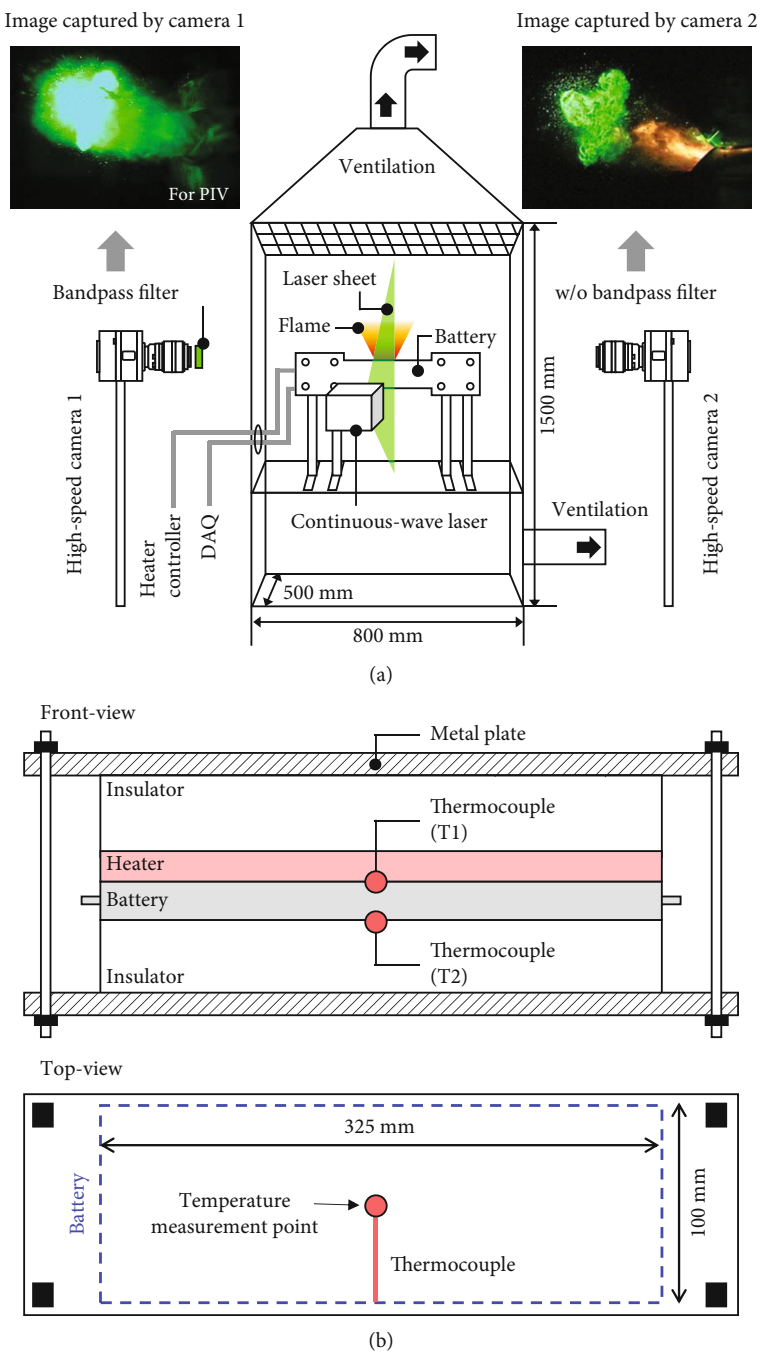

Figure 1: Schematic of the experimental setup for thermal runaway evaluation: (a) open-type acrylic chamber and (b) heating system for thermal abuse of a lithium-ion battery.

abuse of a single-charged cell. The open-type acrylic chamber, visualization technique, and image processing method used in the visualization experiment are described in detail.

2.1. Experimental Setup. BTR visualization is difficult due to the large amount of gas that is ejected and the speed at which the visualization chamber fills with gas. Ejected gas degrades image quality, limiting quantitative analysis. In this study, an acrylic chamber larger than a general constant volume chamber was fabricated for BTR visualization. Because it is an open-type chamber, sufficient oxygen was available inside the chamber. In addition, the chamber was ventilated after image acquisition to prevent flow from affecting the BTR process. Ten NCM 811 batteries ($325 \times 100 \times 9.5\,\mathrm{mm}^3$) were evaluated. The test batteries had a rated voltage of 3.7 V and a capacity of 56.2 Ah. The state of charge was 100% in all BTR experiment (constant current-constant voltage charging). A profile of battery charging condition is tabulated in Table 1. A detailed schematic of the experimental setup is shown in Figure 1.

Table 2: Details of experimental equipment.

Items	Details
Battery charger	800 W, 70 Ah, 5 V 0.05% FS (voltage), 0.1% FS (current)
Heater	220 V, 600 W Maximum temperature: 600°C Size: $300 \times 100 \times 2\,mm^3$
NI 9239	4 channels Resolution: 24 bits Accuracy: 0.03%
NI 9214	16 channels Resolution: 24 bits Accuracy: 0.04%
Continuous wave laser	Wavelength: 532 nm Power: 15 W 3% power stability and 10 kHz modulation
Camera	With bandpass filter: VEO 710 L, Phantom Without bandpass filter: VEO 1310, Phantom

The acrylic chamber had a volume of $6 \times 10^6\,cm^3$ (1500 mm × 800 mm × 500 mm), and acrylic plates 5 mm thick were applied to the front, left, and right sides. Acrylic plates were not directly exposed to the flame generated during BTR, so that plates were not melted. However, solid particles, debris, and soot generated during the combustion process stuck to the acrylic surface. This phenomenon deteriorates image quality, so that acrylic plates were replaced periodically. A checkerboard-style wire mesh was applied to the upper surface of the chamber to prevent damage to the exhaust line from particles ejected during thermal runaway. A laser sheet was formed at the initial gas ejection position using a continuous wave laser (532 ns, 15 W output) and convex and concave lenses. The BTR process was photographed using high-speed cameras on the left and right sides of the acrylic chamber. A bandpass filter (532 nm ± 10 nm) was applied to one high-speed camera to capture only the 532 nm wavelength, and BTR was quantitatively evaluated by applying the PIV to the particles (solids and droplets) ejected. To generate BTR by thermal abuse, the system was configured as shown in Figure 1(b). A flat heater ($300 \times 100 \times 2\,mm^3$, 600 W) was installed, and thermocouples were attached to the upper and lower surfaces of the battery to measure temperature change over time at the center of battery. The heater area was approximately 92% of the battery surface area. Because a pouch-type battery expands when heated, the contact area with the flat heater was reduced such that smooth heat transfer was not possible. To compensate, insulators and metal plates were attached to the upper and lower surfaces of the battery and heater and fixed with bolts. A heating rate of 10°C/min was maintained by minimizing the decrease in heat transfer due to battery swelling. Temperature data were measured using an NI 9214, and experiments were performed in synchronization with a heater controller and camera. The voltage of the battery was measured with an NI 9239. Details of the equipment are described in Table 2.

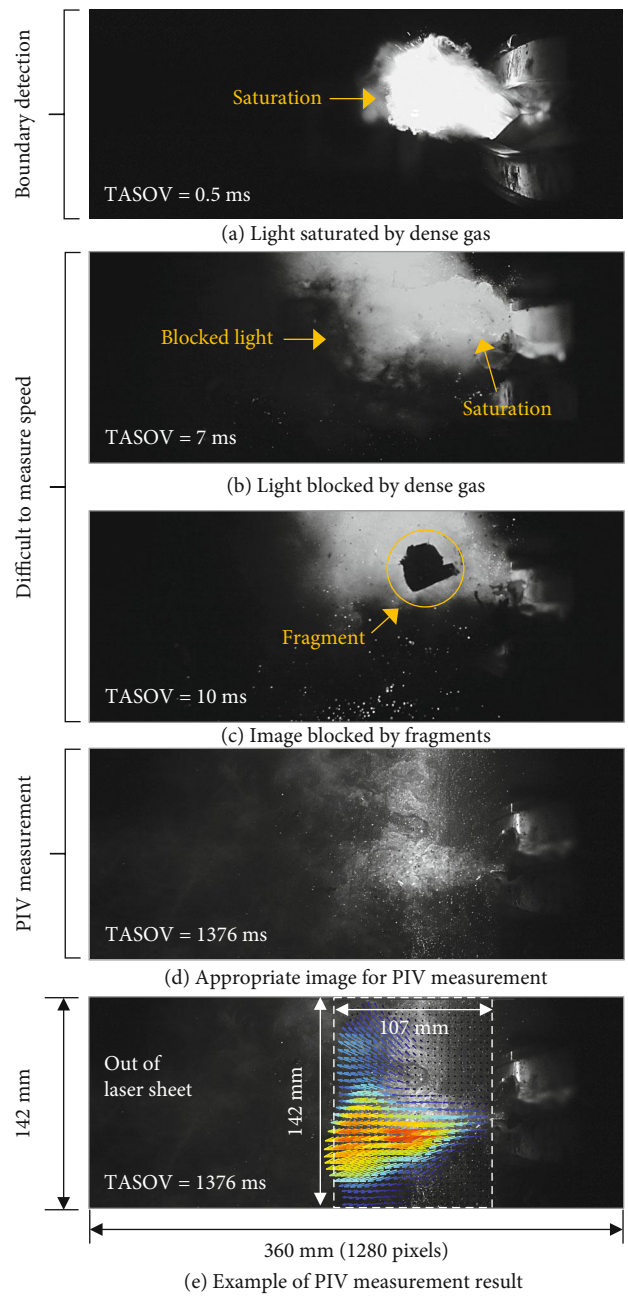

Figure 2: Characteristics of BTR images for measuring venting speed.

2.2. Quantitative Indices

2.2.1. Venting Speed. In this study, venting speed was measured using PIV and a boundary detection method to quantify characteristics of BTR. PIV measurement is a nonintrusive technique that visualizes and quantifies fluid flow patterns. It provides detailed information about the velocity field of a fluid by analyzing the movement of small tracer particles suspended in the flow. In the process of thermal runaway of a lithium-ion battery, evaporated electrolyte is ejected in the form of an aerosol inside the battery. Solids ejected at the same time can be used as tracers to quantify venting speed by applying the PIV technique. However, application of PIV has limitations due to the large amounts of gas, flame, and fragments and

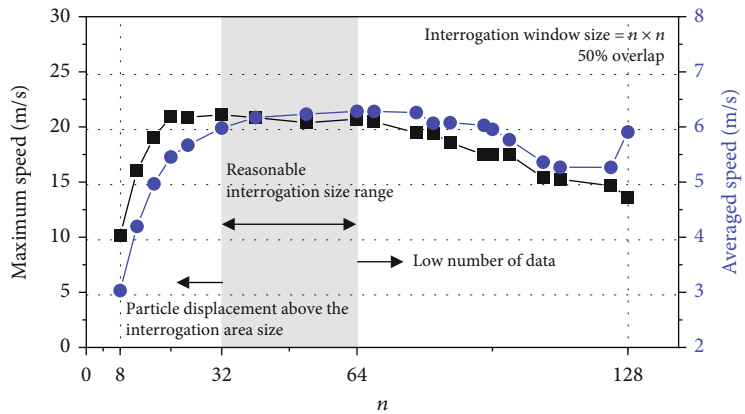

Figure 3: Maximum and average speeds for interrogation window size.

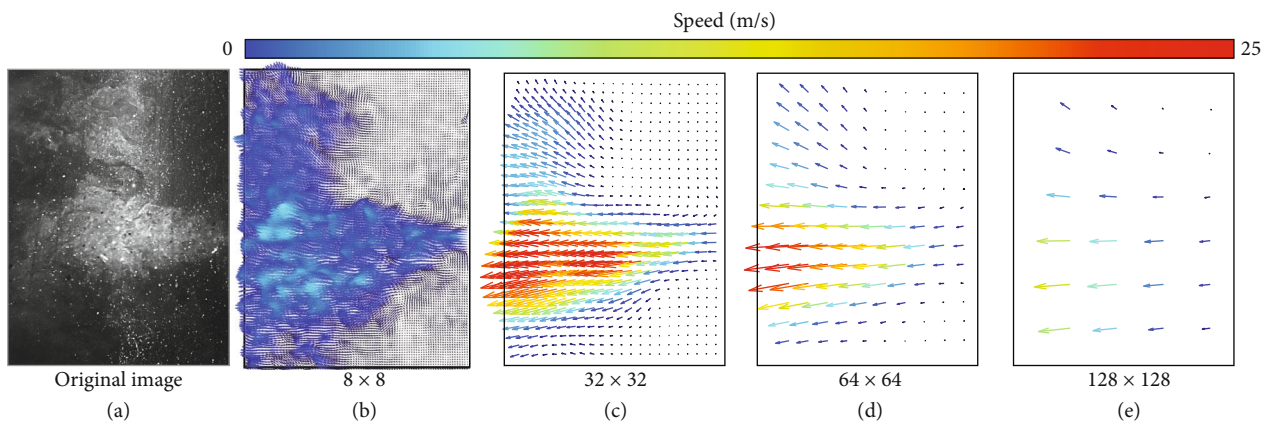

Figure 4: Sample PIV measurements.

Table 3: Specifications of the PIV system.

Items	Details
Camera	High-speed camera (VEO 710 L, Phantom)
Laser	Continuous wave laser (532 nm wavelength, 15 W)
Region of interest	107 × 142 mm
Resolution	380 × 504 pixels
PIV image time interval (dt)	50 μs
Frame rate	20,000 fps
Exposure time	20 μs
Interrogation area	64 × 64 pixels (18 mm × 18 mm, 50% overlap) 32 × 32 pixels (9 mm × 9 mm, 50% overlap)
Correlation algorithm	Fast Fourier transform

the direction of ejected gas. Figure 2 depicts the BTR process over time, whether the PIV technique can be applied, and how to measure the venting speed. Immediately after the seal of the battery is disrupted, a large amount of electrolyte is ejected to the outside due to the large amount present inside the battery, as shown in Figure 2(a). The high gas density saturates the light and limits the use of PIV. In this case, the venting speed—"distance divided by time"—can be measured as the gas ejection distance. Due to the large amount of gas, light is blocked, creating a shadow, and in this case, light saturation occurs due to the high density of the gas, as shown in Figure 2(b). In addition, debris generated when a battery cell is damaged can be photographed, as depicted in Figure 2(c). In situations such as those in Figures 2(b) and 2(c), PIV cannot be applied. Because the gas is continuously ejected beyond the regions of interest, it is difficult to determine the boundary and measure the speed based on the distance or to apply both boundary detection and PIV until the gas flow rate decreases. When the gas flow rate decreases over time, distinguishable electrolyte droplets and solids are ejected, as shown in Figure 2(d), and the venting speed can be measured by evaluating the image. As the vent gas is ejected at a random angle, it is difficult to select an appropriate location for the laser sheet. We fixed the laser sheet to the center of the cell, where the pouch was most likely to be torn. Images were evaluated only when vent gas was present in the laser sheet. As a result, PIV measurement was successful, as shown in Figure 2(e).

Figure 3 shows the maximum and spatially averaged speeds according to the size of the interrogation window.

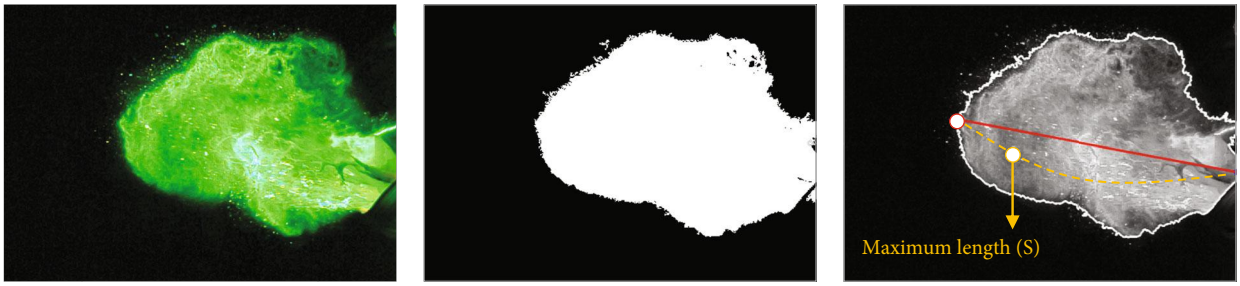

(a) Original image (b) Binarized image (c) Detected boundary image

Figure 5: Image processing in boundary detection.

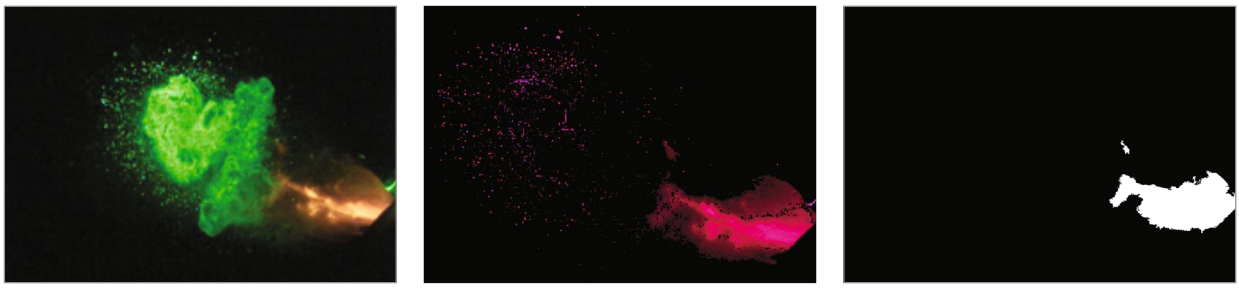

(a) Original image (b) Filtered image (c) Binarized image

Figure 6: Image processing for calculating flame area.

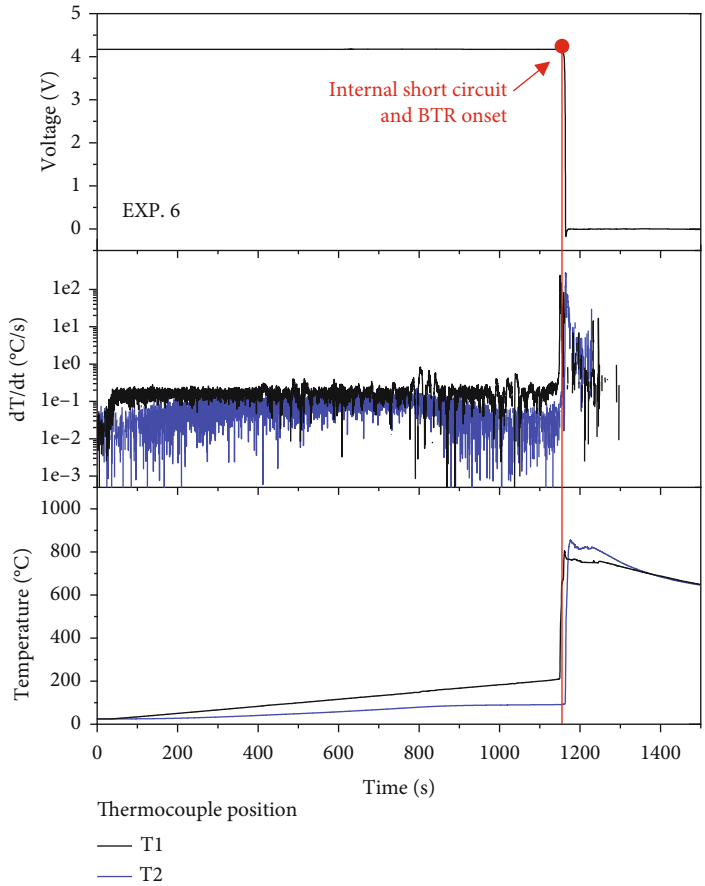

Figure 7: Voltage, temperature rate, and temperature profile during the experiments.

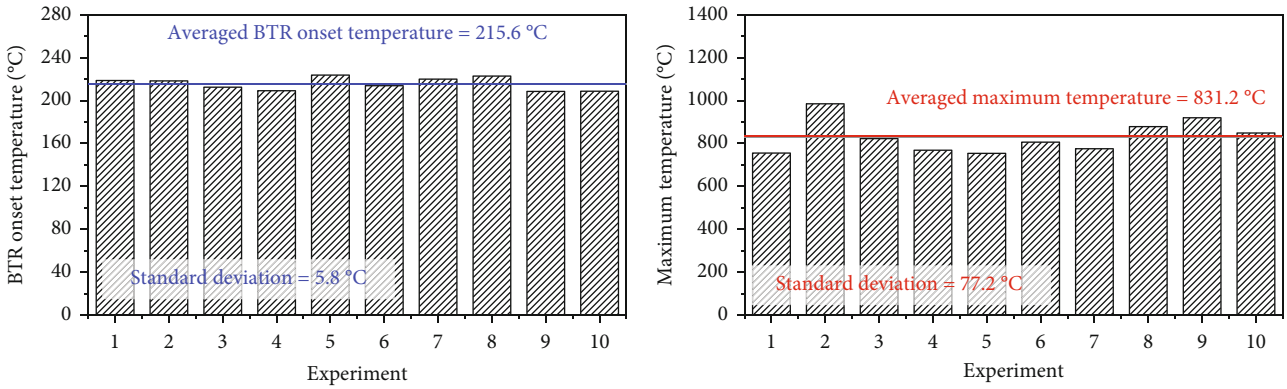

(a) BTR onset temperature

(b) Maximum temperature

Figure 8: BTR onset and maximum temperatures at thermocouple position T1.

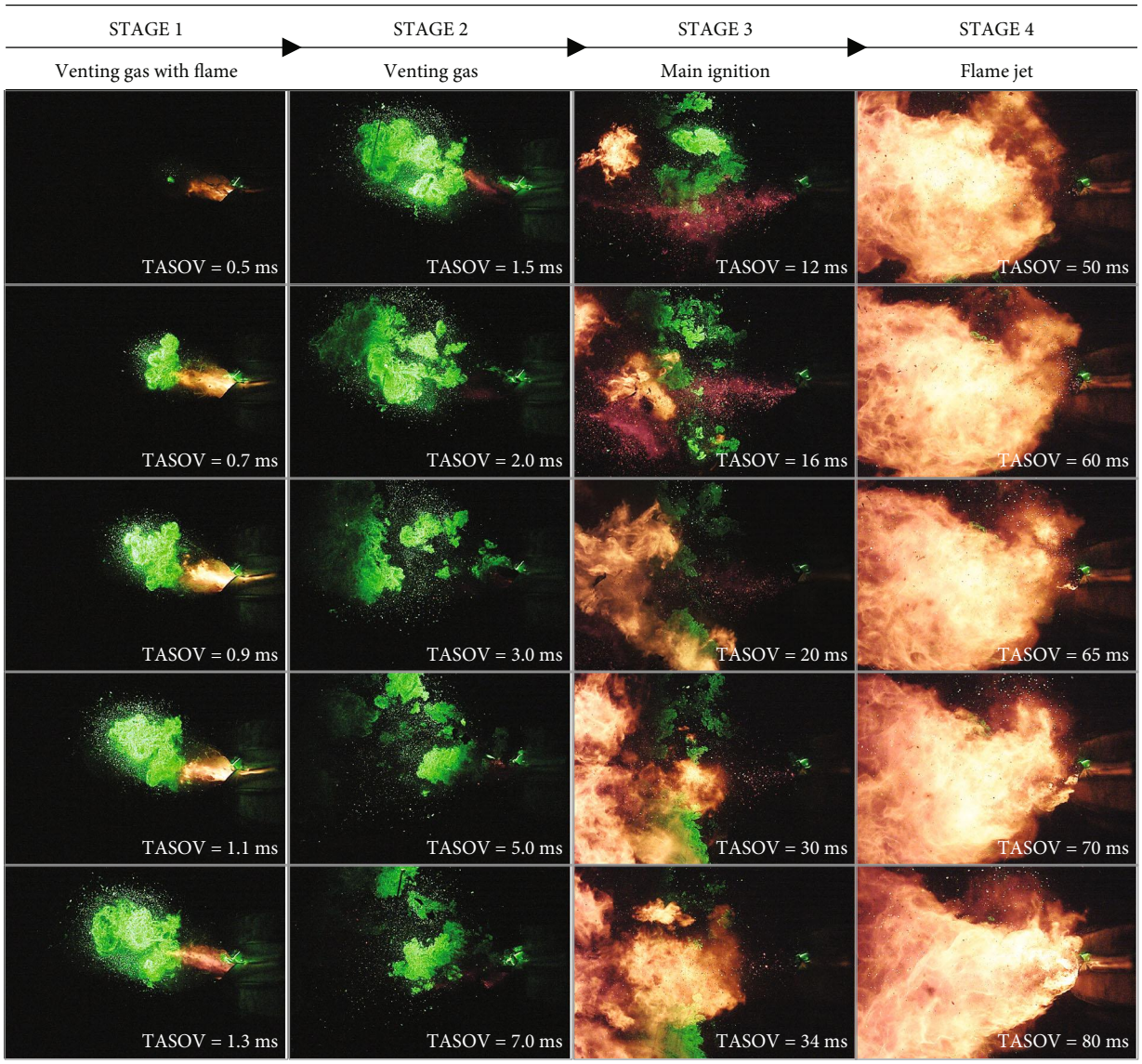

Figure 9: External ignition mechanism of the BTR process (experiment 2).

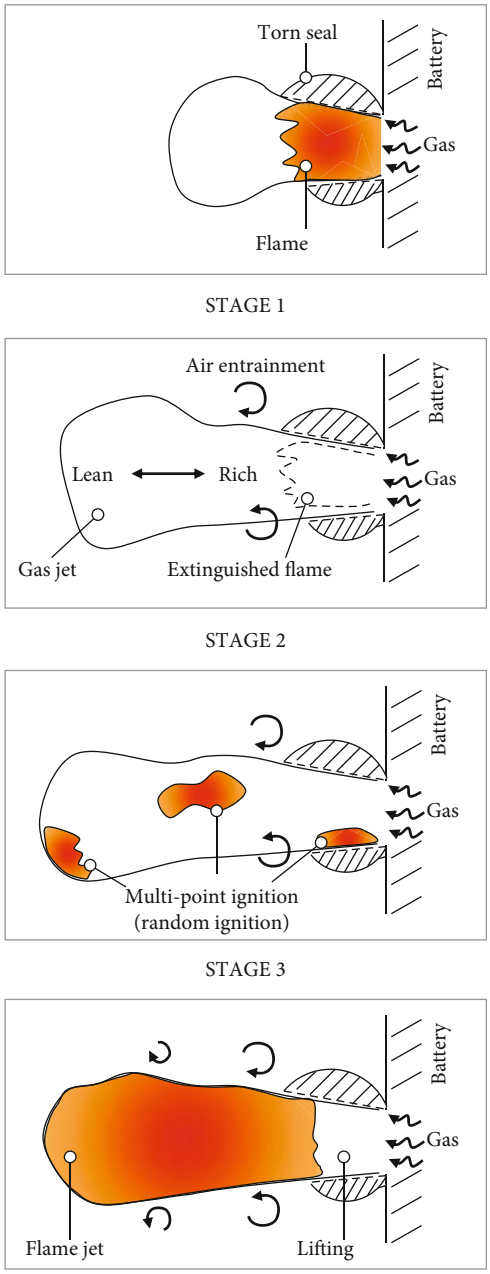

Figure 10: Schematic of the BTR process.

Both the maximum and average speeds converged in an interrogation window size between 32×32 and 64×64, and the maximum speed is shown. The average and maximum speeds decreased as the interrogation window size became smaller than 32×32. Keane and Adrian [56] recommended an interrogation window size four times larger than the local mean particle image displacement. As the interrogation window size decreased, the valid detection probability decreased due to violation of the "one-quarter rule." However, if the interrogation window size increased, the number of data points (vectors) decreased, hindering analysis of the flow characteristics as shown in Figure 4. PIVLab [57], MATLAB software, was used to evaluate images. The traditional PIV uses pulsed lasers. Therefore, timing and synchronization errors can occur during image acquisition, but these errors were minimized in this study by using a high-energy continuous wave laser and high-speed camera. In addition, distortion and diffuse reflection on the surface of acrylic plate were minimized by using a camera and lens with a greater depth of field than thickness of laser sheet. Since the acquired vector contains errors and the actual flow velocity is unknown, standard images are used to evaluate the accuracy of the algorithm. The bias error of the PIVLab algorithm used in this study is less than 0.005 pixels and the random error is less than 0.02. Considering the size of the interrogation window, image time interval, and dynamic range (maximum speed of 180 m/s), the particle displacement is less than 25% (2.25 mm) of the interrogation window. The measured speed data is a result derived from ejected solids and liquid droplets. Even if ejected at the same pressure, the initial momentum and drag influence are different due to the difference in mass. Therefore, the measured data are not representative of the venting gas speed. However, based on the actual ejected solids and liquid droplets, the velocity of the main flow in the measurement plane can be indicated. The ejection speed of gas, solid particles, droplets, and flames during the BTR can be roughly inferred through measured results. The details of the PIV system are described in Table 3.

Figure 5 shows the image processing involved in measuring the speed using the boundary detection method. The original image, Figure 5(a), was converted to a binarized image, Figure 5(b), and the boundary of the vent gas was derived based on that image. Based on the ejection outlet where the seal of the battery cell was torn, the longest distance was selected as the maximum length (S). The ejection velocity can be calculated as $\Delta S/\Delta t$. The value Δt is the camera shutter speed. Because this method calculates the distance by deriving the boundary to measure the speed, it is possible to measure the speed only for a relatively short section immediately before exiting the region of interest. The initial ejection speed was relatively rapid, and the ejectate quickly passed through the visible region. In this study, the ejection velocity was measured using the boundary detection method until 0.9 ms after the start of venting. Afterward, PIV was applied, the venting gas flow rate decreased, and light saturation did not occur.

2.2.2. Flame Area. In this study, flames were measured to quantify the characteristics of the BTR process. Figure 6 shows the image processing sequence used to calculate flame area. Based on the original image, Figure 6(a), the flame was extracted by filtering, as shown in Figure 6(b). The filtered image was converted to a binarized image, as in Figure 6(c). Flame area was derived by calculating the number of white pixels.

3. Results and Discussion

In this study, the BTR characteristics are quantified and analyzed based on the results of thermodynamic analysis and visualization based on temperature data. The results are discussed in detail in a subsequent section.

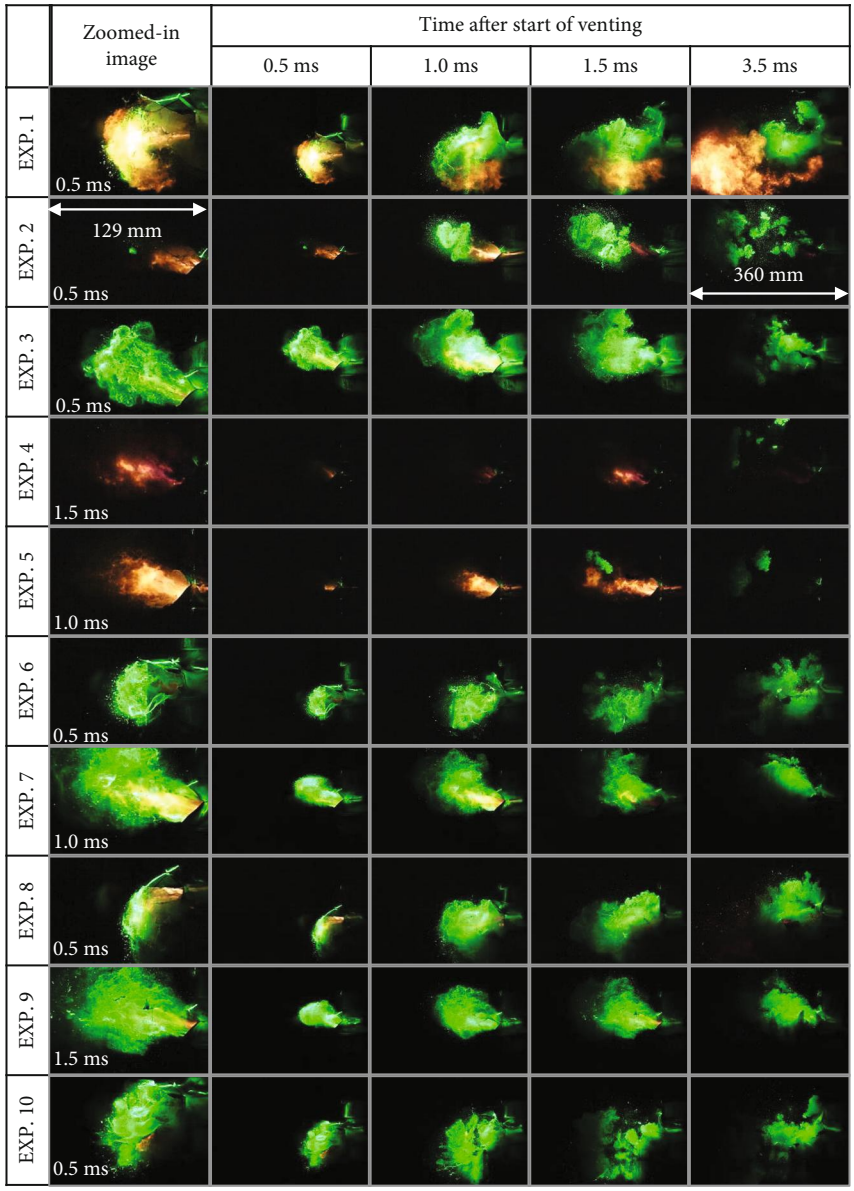

Figure 11: Initial stage right after the battery seal was torn (stage 1).

3.1. Thermodynamic Results. In this section, the temperature characteristics during BTR under thermal abuse conditions using a heating plate are analyzed.

The battery voltage, temperature rate, and temperature under the conditions involved in raising the heating plate energy to increase the battery temperature at 10°C/min are shown in Figure 7. Temperature T1, measured at the thermocouple between the battery and the heating plate, rose 10°C/min until BTR. Temperature T2, measured at the thermocouple where the battery contacted the ambient air, was affected by conduction within the battery cell and convection with the ambient air such that it increased relatively slowly compared with T1. As the battery cell temperature increased, the first reaction that occurred inside the cell was solid electrolyte interphase decomposition on the anode. This reaction takes place at a relatively low temperature of 69°C [58]. Subsequently, as the temperature gradually increases, reactions between the anode and electrolyte and between the cathode and electrolyte, electrolyte decomposition, and binder reactions occur [21, 59]. In addition, separator melting during exothermic reactions created a short circuit between electrodes. Eventually, breakdown of the electrolyte and cathode leads to a rapid release of heat inside the battery [60]. The internal short circuit and rapid temperature rise appeared almost simultaneously. In addition, when the pressure inside the battery increased due to the gas generated by the reaction of the battery materials and electrolyte evaporation, gas and materials were ejected. After reaching the maximum temperature, the battery temperature decreased through the release of energy during venting.

The critical temperatures for BTR analysis include BTR onset temperature and battery cell maximum temperature. In this study, the BTR onset temperature, which was defined as the temperature at the point where the temperature

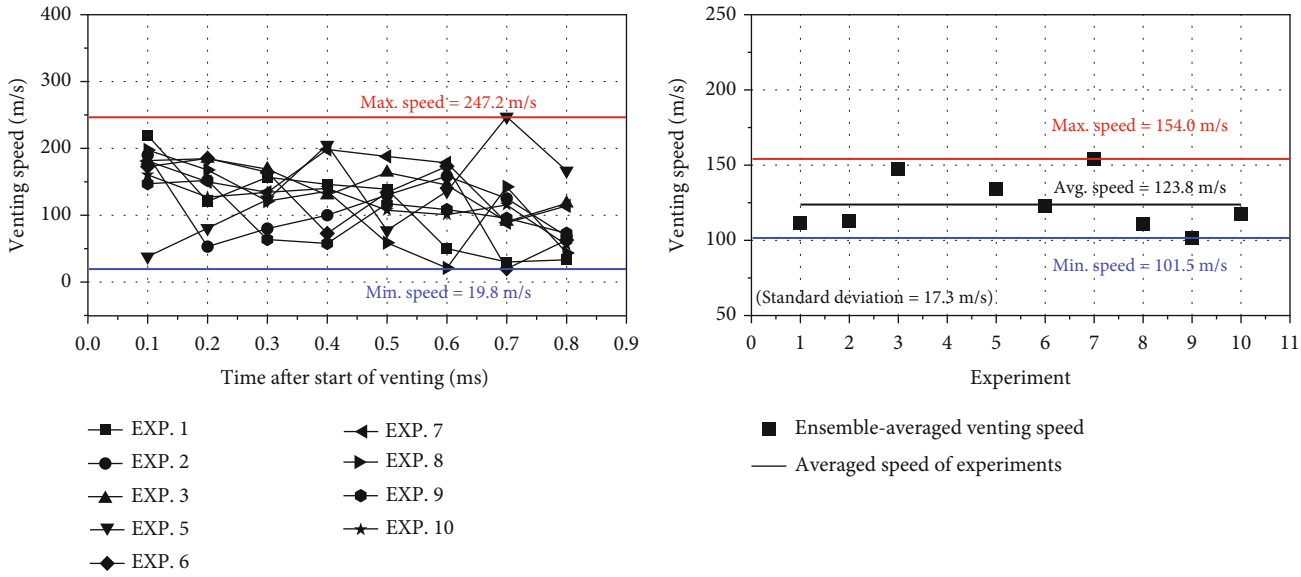

(a) Venting speed for time

(b) Averaged venting speed

Figure 12: Venting speed in stage 1.

increased by 10°C/s or greater, was determined first. Figure 8 shows BTR onset and maximum temperatures. In the experiments, the BTR onset temperature ranged from 208 to 223°C, with an average of 215.6°C. The maximum temperature averaged 831°C. The maximum temperature range was from 818 to 1047°C. The difference depending on the experiments was larger than the BTR onset temperature because the pouch-cell swelling, reaping, and venting associated with the gas and material ejection process were relatively random compared with other battery types. In addition, there is also an effect of the increase in the variability of the BTR of the battery using the cathode material with a high nickel content [61] used in this study. The thermocouple used in the experiment was attached to the central surface of the battery. However, because the degree of contact with the surface can vary during the battery expansion and explosion process, errors can be included in the measured temperature data. Additionally, factors that increase the randomness of thermal runaway include unidentifiable factors such as variations in the battery manufacturing process and a series of chemical reactions that occur inside the cell. Therefore, the measured temperature data contains errors. The onset temperature and maximum temperature are affected by various factors such as battery capacity, surrounding environment, heating rate, and battery material. Even considering the different experimental conditions, the results of this study are reasonable comparable with the results of previous studies. Wei et al. [62] conducted experimental study on BTR characteristics of various lithium-ion batteries with specifications including capacity, cathode material, and package type. They confirmed that the onset temperature was around 140 to 175°C or various NCM batteries with capacities from 51 to 115 Ah. This was reasonable considering that the melting point of the separator material was 166°C. The maximum temperature range was from 555 to 1066°C. A study performed by Yuan et al. [63] also showed similar results. They conducted their study on relatively low-capacity NCM batteries (3.2 Ah). The measurement results showed an onset temperature of 140 to 145°C and a max temperature of 845 to 998°C. Damage to the separator reduces the physical separation effect between the anode and cathode and releases significant electrical energy when an internal short circuit occurs, resulting in an unstoppable BTR. Therefore, the material of the separator can greatly affect the onset temperature. The separator coated by ceramic can maintain its structural integrity, resulting in the onset temperature over 200°C [64]. Therefore, many studies have reported that the possibility of fatal BTR increases at temperatures over 200°C.

3.2. External Ignition Mechanism under Thermal Abuse Conditions. Figure 9 visualizes the results of BTR over time. Figure 10 is a schematic of the external ignition mechanism of BTR during thermal abuse. The chosen BTR process was the best representation of the 10 battery cell visualization results and was divided into four stages. In stage 1, the seal of the battery cell was torn, and the electrolyte was ejected in the form of an aerosol with flames. In stage 2, only the venting gas was ejected from 9 out of 10 battery cells. The flame was extinguished due to the high venting speed and high venting gas concentration. In one test battery cell, the flame generated in stage 1 propagated without being extinguished. Because the results were derived based on 10 battery cells, a statistical approach is difficult, but when compared to previous research results, it is clear that the ejection of combustible gas precedes the occurrence of a serious fire. In stage 3, flames that ignited randomly at multiple points propagated rapidly to the surrounding vent gas. In stage 4, the flame was fully developed, and lifting occurred repeatedly at the jet outlet. In addition, the fully ignited flame was not extinguished. The angle, area, and direction of the flame changed continuously over time.

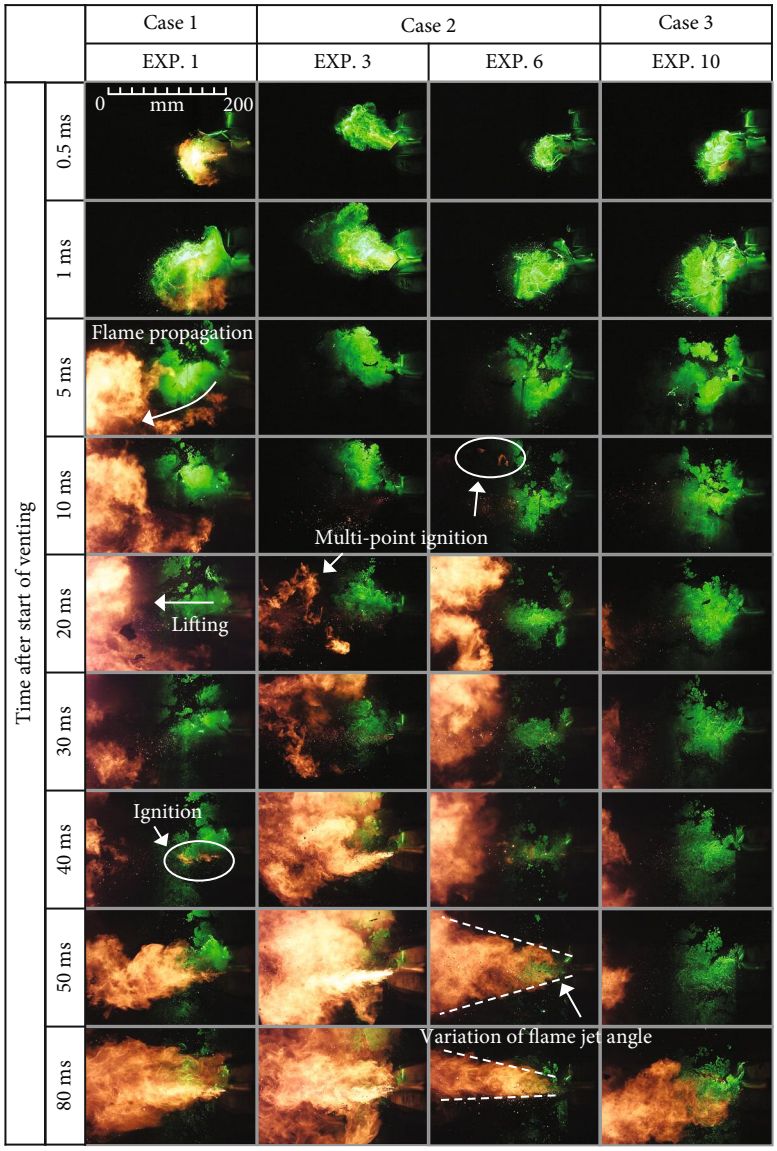

Figure 13: BTR process from stage 2 to stage 4.

Figure 11 shows the initial stage immediately after tearing of the seal in all 10 batteries. Vent gas was ejected in different shapes and directions for each cell, and all produced flames. Ignition was possible due to the continuous temperature increase and the presence of oxygen inside the cell during thermal runaway of the battery [65, 66]. At stage 1, experiment 1 showed a difference compared with other repeated experiments: the flame in the initial stage was relatively wide and surrounded the vent gas.

Figure 12 shows the venting speed 0.8 ms after venting and the ensemble-average venting speed for each experimental case. Experiment 4 was not included in the results because the direction of the gas ejection deviated from the laser sheet at the initial stage and speed measurements could not be performed. For approximately 0.8 ms after the seal was torn, vent gas was ejected from the 10 battery cells at speeds between 19.8 and 247.2 m/s, as shown in Figure 12(a). When the cell pouch burst, the internal pressure dropped rapidly, and the outlet diameter changed continuously, deforming the pouch and creating an irregular and wide range of speeds, from a minimum of 101.5 m/s to a maximum of 154.0 m/s, as shown in Figure 12(b).

Beginning with stage 1, flames formed three major shapes (Figure 13). In case 1, the flame ejected along with the vent gas in stage 1 was not extinguished. Rapid and immediate flame propagation followed the edge of the gas jet, and the flame expanded to a large area in a well-mixed air-fuel (ejected electrolyte) mixture in front of the gas jet. The flame at the front of the gas jet could not propagate in the direction of the ejection outlet and was lifted and pushed out by the gas jet. Ignition occurred inside the gas jet, and the flame propagated rapidly to form a complete flame jet. This phenomenon was observed from 1 out of 10 battery cells. In case 2, the flame emitted with the vent gas was extinguished within a short time. Immediate ignition did not occur while the vent gas was ejected but after approximately

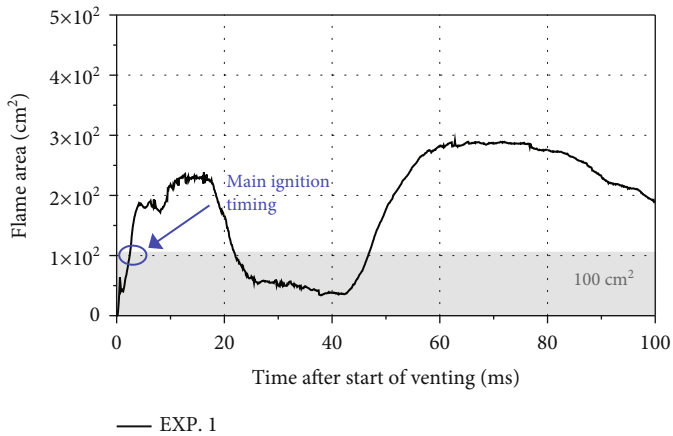

(a) Case 1

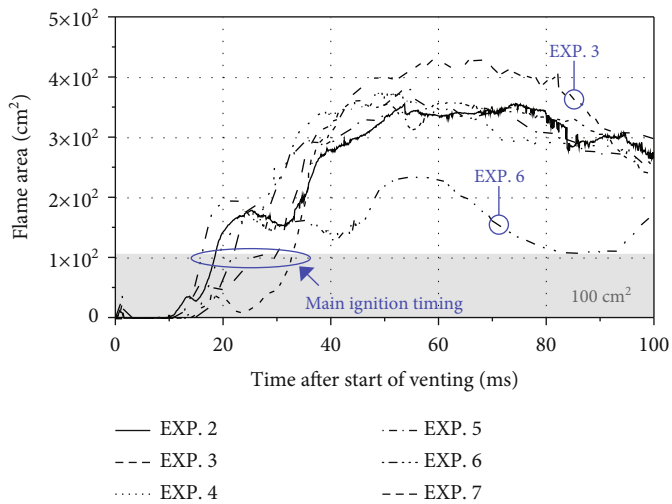

(b) Case 2

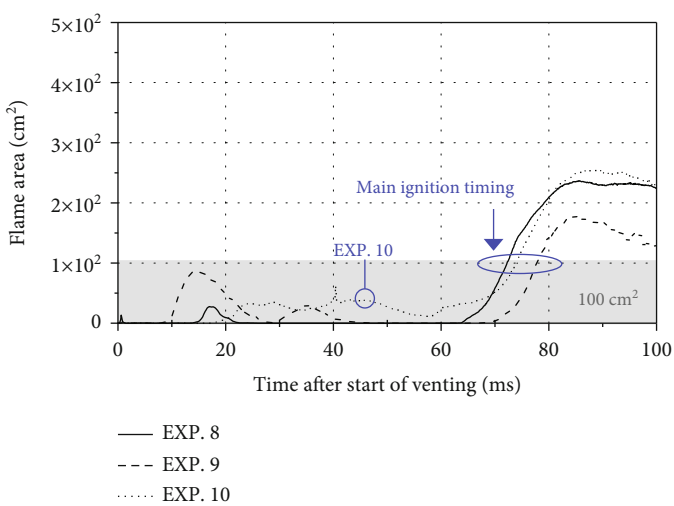

(c) Case 3

Figure 14: Flame area.

10 ms, and the flame propagated. The cause of ignition is thought to be the temperature increase resulting in spontaneous ignition of the high-temperature solid [55] ejected with the gas. The expanded flame was not extinguished but continued to increase the ambient temperature and propagate further. As a result, only repeated lifting formed a flame

jet. Experiments 3 and 6 formed flame jets in the same way, but the flame jet angle increased and decreased repeatedly in experiment 6. The ejection outlet area, the pressure inside the cell, and the angle of the torn pouch changed continuously. In case 3, the flame ejected along with the gas was extinguished as in case 2. Afterward, ignition occurred at the front of the gas jet, but the flame did not propagate for a relatively long time (more than 50 ms). After that, a flame formed and propagated inside the gas jet to form a flame jet.

Figure 14 shows the flame area over the period following vent gas ejection. As described above, in case 1, the flame grew simultaneously with the eruption. The flame area decreased after approximately 18 ms but then grew rapidly after 40 ms due to ignition inside the gas jet. In case 2, the flame erupted after the seal was torn but was extinguished within a short time. A second flame grew through simultaneous ignition and flame propagation processes approximately 10 ms later. In case 3, flame growth was relatively slow, starting at 60 ms. In all 10 experiments, the flame continued without extinguishing after covering an area of approximately 100 cm^2. In this study, the point at which the flame area exceeded 100 cm^2 was defined as the main ignition timing (MIT). MIT as defined in this study is influenced by several factors. MIT can be affected by definition and visualization area size. For example, if the flame area is defined to be smaller, the MIT is advanced. Additionally, unextinguished flames may exist outside the visible area. Therefore, MIT may change if visualized in a wider area. Finally, the measured MIT includes the randomness of thermal runaway. Randomness is caused by various reasons such as vent gas angle, speed, degree of tearing of the seal, and air-fuel mixing characteristics. However, despite this influence, MIT was defined for objective analysis of the thermal runaway process by minimizing the researcher's subjectivity.

Figure 15 depicts MIT for the 10 battery cells. In case 1, the flame spread to more than 100 cm^2 in approximately 2.5 ms. The previous results show that in all test battery cells, the first flame is observed immediately after the seal is torn due to internal ignition or external ignition by hot particles. In case 1, immediately after the seal was torn, the gas jet ignited and the flame propagated rapidly (see Figures 11 and 13). In outskirts of the gas jet, air-fuel mixing is promoted, and an equivalence ratio suitable for ignition can be secured. In case 1, despite the high speed and high concentration of gas jet discharge, the flame did not be extinguished. The flame propagated along the outer edge of the gas jet, resulting in short MIT was observed. As a result, in case 1, the flame spread to more than 100 cm^2 in approximately 2.5 ms. In case 2, it took an average of 22.25 ms for the flame ejected with the vent gas to reignite after being extinguished and expand to an area of at least 100 cm^2. In case 3, there was successful ignition, but the flame did not fully propagate, and lifting occurred. After approximately 74.8 ms, a stable flame was ignited and grew. Case 3 involved an ignition delay of approximately 3000% compared with case 1 but, due to the rapid flame propagation, showed a similar level at 100 ms after venting regardless of MIT (Figure 14).

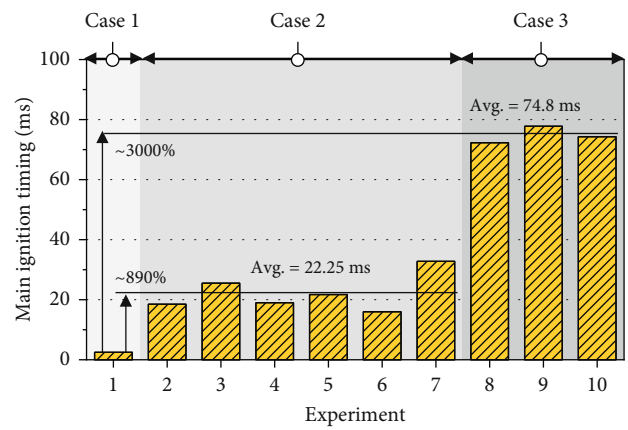

Figure 15: MIT.

We confirmed the difference of MIT between case 2 and case 3 from captured images near MIT. Figure 16 shows flame propagation over time near MIT. Figure 17 shows zoomed-in images at MIT to observe solid particles clearly. The difference in MIT between case 2 and case 3 is believed to be due to the concentration and distribution of high-temperature particles that can become an ignition source. High-temperature particles can act as an ignition source when emitted together with combustible gases. In addition to the emission process of a large amount of solid particles, bright solid particles (hot particles) were clearly observed around the ignition point. It is known that solid particles that can be generated when BTR occurs include metal elements such as Al, Cu, Ni, Co, C, P, S, and Mn, as well as carbon, carbonate, metal oxide, and aromatic compounds [67]. MIT was on average about 50 ms faster in case 2 than in case 3 (Figure 15). In case 2, it was confirmed that lots of pink-colored solid particles (containing lithium) were released widely. This was distinct from the orange-colored flame. As shown in experiment 4 in Figure 17, ignition occurred simultaneously around the released solid particles. On the other hand, in case 3, the released solid particles were not clearly observed compared to case 2. The large number of solid particles and their wide distribution increase the possibility of ignition. Therefore, case 2 showed a shorter MIT than case 3 (approximately 50 ms). As a result, in case 3, ignition occurred as the venting speed and flow rate of vent gas decreased and air-fuel mixing increased. In both case 2 and case 3, multipoint ignition occurred, but in case 3, ignition occurred around the gas jet resulting in a flame jet. However, in terms of safety assurance time, it cannot be concluded that case 3, in which MIT was delayed, is safer than case1 and case 2 because a flame jet is formed within a very short time (less than 0.1 s). In conclusion, regardless of the ignition mechanism, flame propagation was rapid during BTR.

The development of a flame after main ignition timing is shown in Figure 18. Because of the direction and speed of the ejected gas, the flame did not propagate behind the pouch. The flame occurred over a wider area than the gas jet due to the strong turbulence generated around the gas jet. The gas jet occurred continuously with repeated

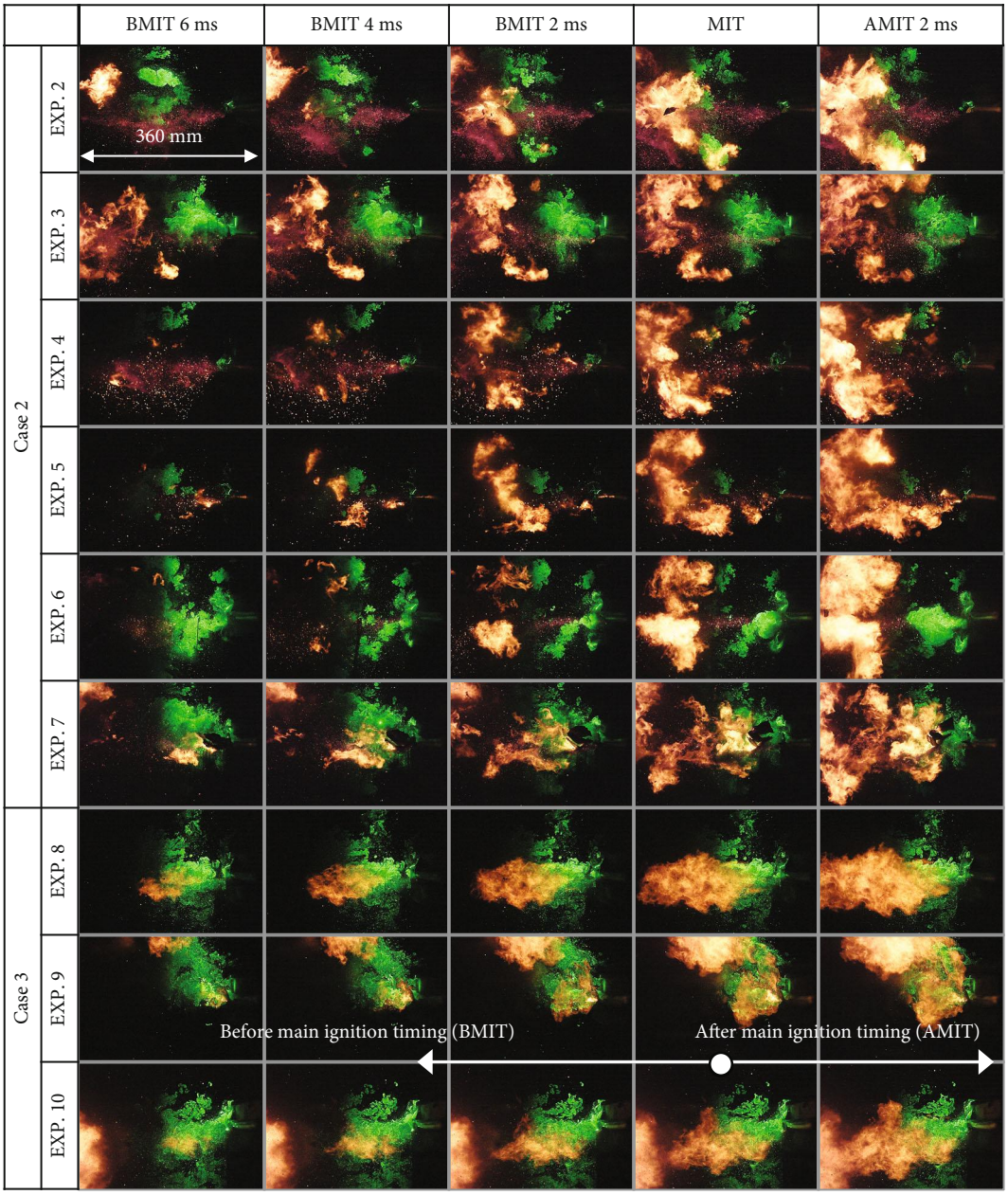

Figure 16: Flame propagation near MIT (stage 3).

evaporation and release of the electrolyte inside the battery cell. During this process, the ejection speed and ejection range changed slightly over time. A strong gas jet introduces ambient air in the gas jet (air entrainment), promotes mixing of fuel (ejected electrolyte) and air, and greatly contributes to flame expansion. However, in our study, the flame could not propagate toward the battery cell due to the formation of a flow in the opposite direction of the battery cell.

Venting speeds over time in experiment 3 are shown in Figure 19. After the cell seal was torn, the venting speed decreased as the pressure inside the cell decreased. Because the average speed was calculated including the stagnant flow field away from the gas jet, it showed a low average speed. As the average speed cannot represent the venting speed, it should be considered along with the vector field and maximum speed results. Experiment 3 produced maximum speeds of approximately 20 m/s after venting, and the maximum speed occurred at the gas jet. The speed in this experiment would not be measured from about TASOV 1 ms to 50 ms. In this region, PIV was not possible due to light saturation caused by a high vent gas flow rate, image quality deterioration caused by impurities, and gas ejection outside the laser sheet. The length of these intervals varied from experiment to experiment because the position and angle of vent gas in a pouch-type cell are random. In the early part of venting when the speed was high, the gas jet was linear. Therefore, if the initial ejection angle deviated from the laser

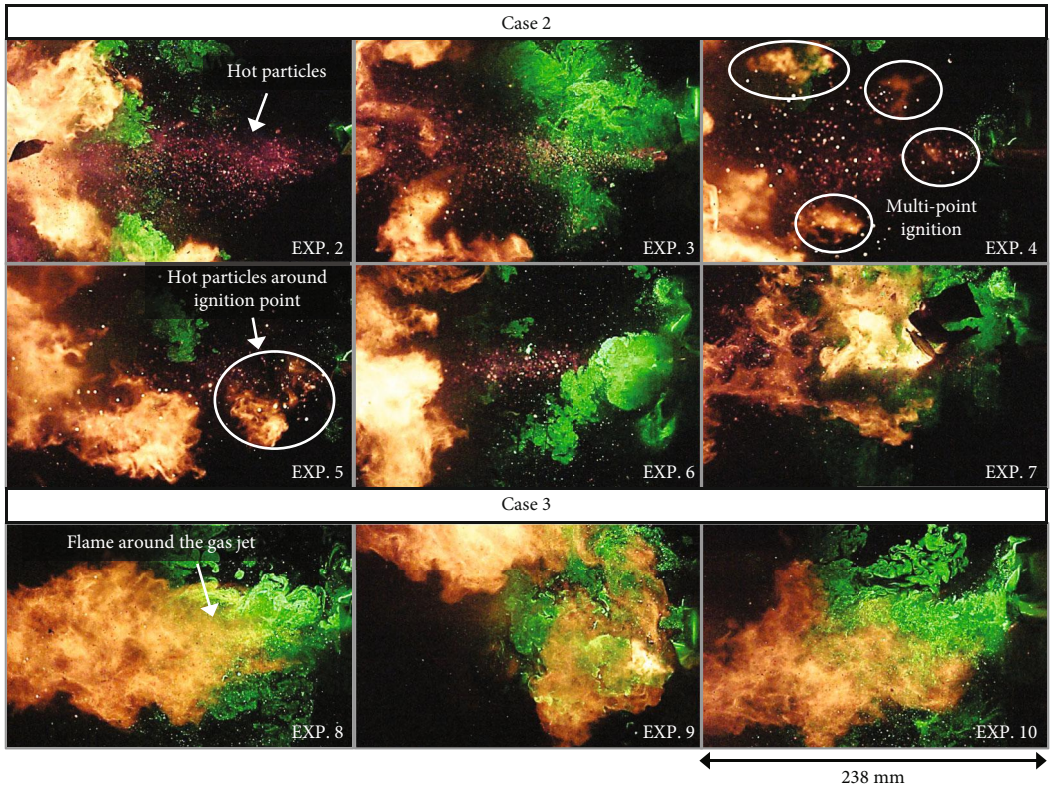

Figure 17: Zoomed-in images at MIT in case 2 and case 3.

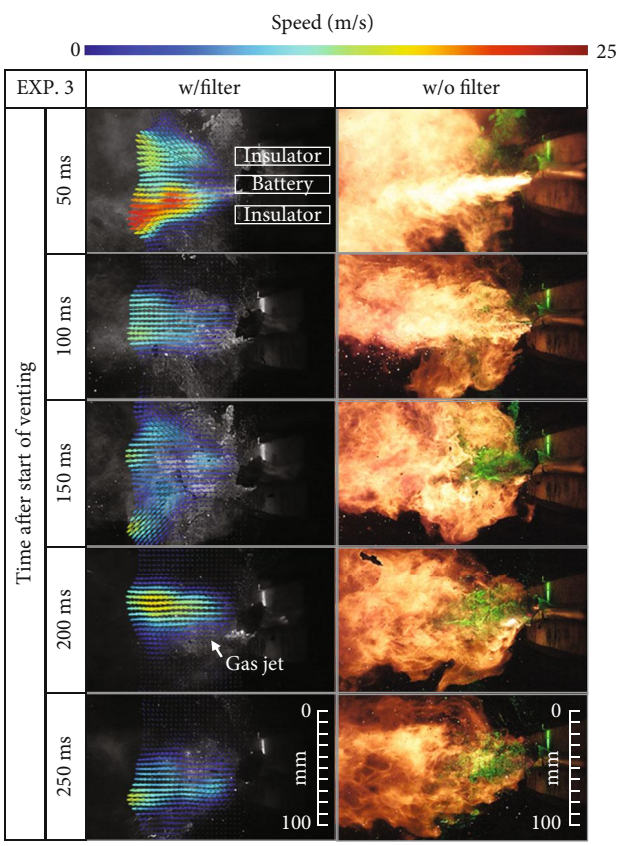

Figure 18: Ensemble-averaged vector fields over time after main ignition timing in experiment 3.

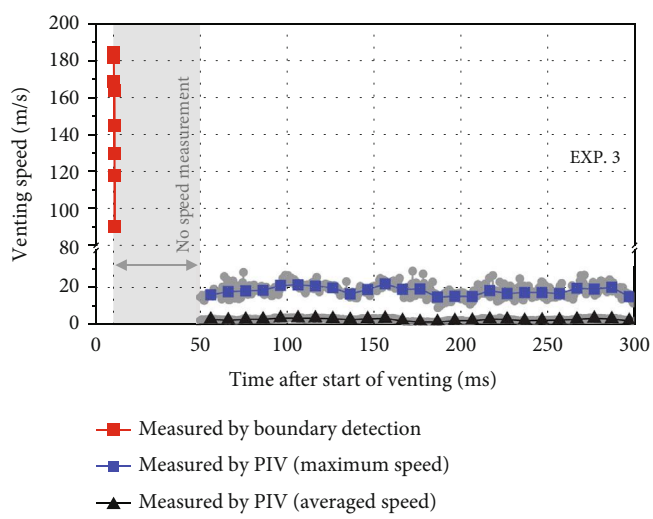

Figure 19: Venting speed over time in experiment 3.

sheet, the gas jet continued to escape the laser sheet until the radial movement increased and the area of the gas jet widened due to the ejection outlet increase. The dominant factors affecting the length of the section in which the speed cannot be measured were the ejection gas flow rate and the ejection angle.

A comparison of the venting speeds for the four experiments showed different flame propagation characteristics among the 10 battery cells, as shown in Figure 20. The results were compared in the region after 1,000 ms, when

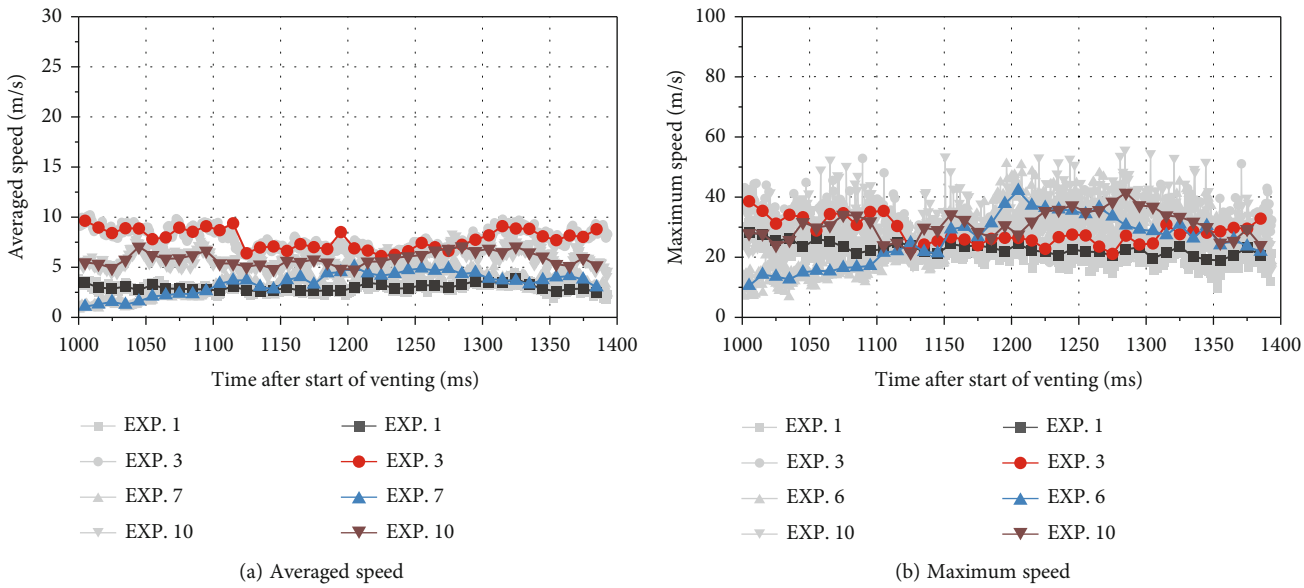

Figure 20: Maximum venting speed measured by PIV. The black, red, blue, and brown colors represent ensemble-averaged speed.

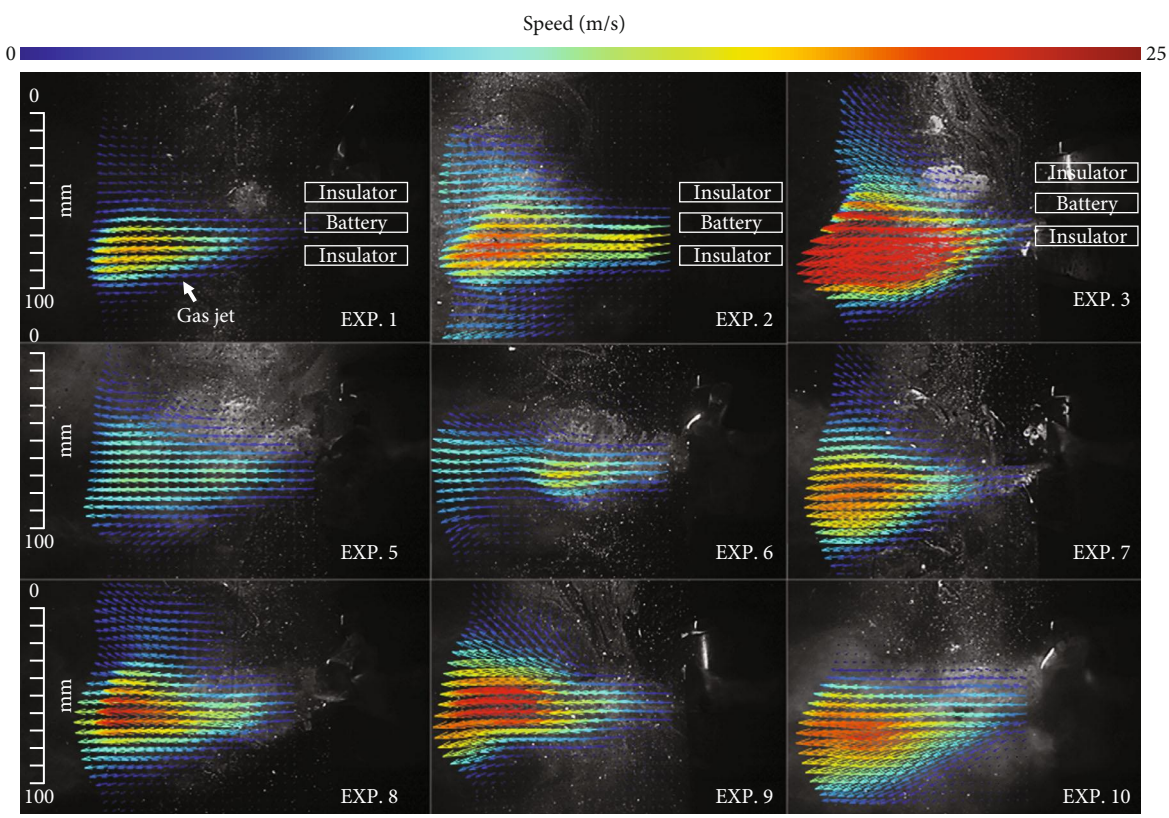

Figure 21: Ensemble-averaged vector fields during BTR (TASOV = 1,100 ms).

the vent gas flow rate was sufficiently reduced such that light saturation did not occur, and the gas jet was located in the laser sheet. Average speeds were low at less than 10 m/s, which was maintained over time, as shown in Figure 20(a). The average speed was affected by vent gas area because the spatially averaged speed was calculated by including the stagnant area around the gas jet. Because the average speed did not closely represent the gas jet speed, maximum speed and vector fields were considered. Maximum speeds were approximately 20 to 40 m/s and were similar over time, as shown in Figure 20(b). In the measurement section, no significant difference or tendencies were found for either the maximum or the average speed because of an unstable region created by rapid pressure drop inside the cell and a

change in the exit cross-sectional area. The repeated pressure increase due to continuous electrolyte evaporation and the pressure decrease due to vent gas ejection formed a gas jet with fluctuations. As a result, despite different maximum speeds at the same time point, structurally similar shapes were evident (Figure 21). In all experiments, the speed decreased as the distance from the center of the gas jet increased.

4. Conclusions

In this study, BTR was quantified using thermodynamics and visualization of thermal abuse conditions for 10 lithium-ion batteries. The BTR process was visualized using two high-speed cameras in an open-type acrylic chamber. The venting speed was measured, and the external ignition mechanism was characterized. PIV and boundary detection were used to measure venting speeds. The conclusions are as follows:

(i) The average BTR onset temperature was 215.6°C and was similar across the 10 lithium-ion batteries. The average maximum temperature was 831.1°C, and the variation between experiments was high compared to the BTR onset temperature due to swelling, repairing, and venting

(ii) External ignition occurred in four stages. In all experiments, the vent gas was ejected along with a flame immediately after the battery cell was torn (stage 1). The flame was extinguished with a probability of 90%, and only vent gas was ejected (stage 2). Multipoint ignition occurred randomly and simultaneously (stage 3), and the flame rapidly propagated and formed a flame jet (stage 4)

(iii) The average venting speed at 0.8 ms after the battery cell seal was torn was approximately 123.8 m/s in the 10 experiments. The pressure decreased inside the battery cell due to the torn battery pouch, the pressure increased due to evaporation of the electrolyte, and the continuous change in exit cross-sectional area due to pouch breakage caused irregular venting speeds

(iv) During BTR, flame propagation and extinction were repeated; after the main ignition timing when the flame area was greater than 100 cm^2, the flame did not extinguish, and a flame jet was formed. However, regardless of the main ignition timing, the flame propagated rapidly and showed a similar flame area at TASOV 100 ms

(v) In the 10 experiments, the structure and speed of the venting gas were similar after a stable flame jet was formed. The core of the gas jet showed the highest speed at 20 to 40 m/s, and the speed decreased as the distance from the jet core increased

This study confirmed the utility of applying PIV to a quantitative evaluation of BTR and secured useful data for simulation model validation. However, BTR characteristics were analyzed for only a small portion of the entire BTR process. Analysis of the BTR process at later time points is required.

Abbreviations

AMIT: After main ignition timing
BMIT: Before main ignition timing
BTR: Battery thermal runaway
MIT: Main ignition timing
NCM: Lithium nickel cobalt manganese oxide
PIV: Particle image velocimetry
SOC: State of charge
TASOV: Time after start of venting.

Data Availability

The data used to support the findings of this study are available from the corresponding author upon request.

Conflicts of Interest

The authors declare that they have no conflicts of interest.

Acknowledgments

This work was supported by the Korea Institute of Energy Technology Evaluation and Planning (KETEP) grant funded by the Ministry of Trade, Industry & Energy (MOTIE) of the Republic of Korea (No. 20224000000440).

References

[1] S. Bouckaert, A. F. Pales, C. McGlade et al., *Net Zero by 2050: A Roadmap for the Global Energy Sector*, International Energy Agengy (IEA), 2021, https://www.iea.org/.

[2] A. García, J. Monsalve-Serrano, R. L. Sari, and S. Martinez-Boggio, "Energy assessment of an electrically heated catalyst in a hybrid RCCI truck," *Energy*, vol. 238, article 121681, 2022.

[3] T. Liu, Y. Liu, X. Wang, X. Kong, and G. Li, "Cooling control of thermally-induced thermal runaway in 18,650 lithium ion battery with water mist," *Energy Conversion and Management*, vol. 199, article 111969, 2019.

[4] J.-C. Feng, J. Yan, Z. Yu, X. Zeng, and W. Xu, "Case study of an industrial park toward zero carbon emission," *Applied Energy*, vol. 209, pp. 65–78, 2018.

[5] A. Nordelöf, M. Romare, and J. Tivander, "Life cycle assessment of city buses powered by electricity, hydrogenated vegetable oil or diesel," *Transportation Research Part D: Transport and Environment*, vol. 75, pp. 211–222, 2019.

[6] C. Zhang, J. Jiang, Y. Gao, W. Zhang, Q. Liu, and X. Hu, "Charging optimization in lithium-ion batteries based on temperature rise and charge time," *Applied Energy*, vol. 194, pp. 569–577, 2017.

[7] H. Zhang, X. Song, T. Xia et al., "Battery electric vehicles in Japan: human mobile behavior based adoption potential analysis and policy target response," *Applied Energy*, vol. 220, pp. 527–535, 2018.

[8] A. M. Andwari, A. Pesiridis, S. Rajoo, R. Martinez-Botas, and V. Esfahanian, "A review of battery electric vehicle technology and readiness levels," *Renewable and Sustainable Energy Reviews*, vol. 78, pp. 414–430, 2017.

[9] Z. Liu and H. He, "Sensor fault detection and isolation for a lithium-ion battery pack in electric vehicles using adaptive

extended Kalman filter," *Applied Energy*, vol. 185, pp. 2033–2044, 2017.

[10] J. Yang, X. Liu, J. Tian et al., "Adhesive nanocomposites of hypergravity induced Co_3O_4 nanoparticles and natural gels as Li-ion battery anode materials with high capacitance and low resistance," *RSC Advances*, vol. 7, no. 34, pp. 21061–21067, 2017.

[11] Y. Wang, C. Liu, R. Pan, and Z. Chen, "Modeling and state-of-charge prediction of lithium-ion battery and ultracapacitor hybrids with a co-estimator," *Energy*, vol. 121, pp. 739–750, 2017.

[12] Y. Wang, C. Zhang, and Z. Chen, "A method for joint estimation of state-of-charge and available energy of $LiFePO_4$ batteries," *Applied Energy*, vol. 135, pp. 81–87, 2014.

[13] X. Lai, Y. Zheng, L. Zhou, and W. Gao, "Electrical behavior of overdischarge-induced internal short circuit in lithium-ion cells," *Electrochimica Acta*, vol. 278, pp. 245–254, 2018.

[14] G. P. Beauregard and A. Phoenix, *Report of Investigation: Hybrids Plus Plug in Hybrid Electric Vehicle*, US Department of Energy, Idaho National Laboratory, Idaho Falls, ID, Report, 5903, 2008.

[15] S. Mallick and D. Gayen, "Thermal behaviour and thermal runaway propagation in lithium-ion battery systems–a critical review," *Journal of Energy Storage*, vol. 62, article 106894, 2023.

[16] J. Liang, Y. Gan, M. Tan, and Y. Li, "Multilayer electrochemical-thermal coupled modeling of unbalanced discharging in a serially connected lithium-ion battery module," *Energy*, vol. 209, article 118429, 2020.

[17] L. He, X. Tang, Q. Luo et al., "Structure optimization of a heat pipe-cooling battery thermal management system based on fuzzy grey relational analysis," *International Journal of Heat and Mass Transfer*, vol. 182, article 121924, 2022.

[18] X. Feng, M. Ouyang, X. Liu, L. Lu, Y. Xia, and X. He, "Thermal runaway mechanism of lithium ion battery for electric vehicles: a review," *Energy Storage Materials*, vol. 10, pp. 246–267, 2018.

[19] T. Yamauchi, K. Mizushima, Y. Satoh, and S. Yamada, "Development of a simulator for both property and safety of a lithium secondary battery," *Journal of Power Sources*, vol. 136, no. 1, pp. 99–107, 2004.

[20] H. Maleki and J. N. Howard, "Internal short circuit in Li-ion cells," *Journal of Power Sources*, vol. 191, no. 2, pp. 568–574, 2009.

[21] R. Spotnitz and J. Franklin, "Abuse behavior of high-power, lithium-ion cells," *Journal of Power Sources*, vol. 113, no. 1, pp. 81–100, 2003.

[22] R. A. Leising, M. J. Palazzo, E. S. Takeuchi, and K. J. Takeuchi, "Abuse testing of lithium-ion batteries: characterization of the overcharge reaction of $LiCoO_2$/graphite cells," *Journal of the Electrochemical Society*, vol. 148, no. 8, p. A838, 2001.

[23] Y. Saito, K. Takano, and A. Negishi, "Thermal behaviors of lithium-ion cells during overcharge," *Journal of Power Sources*, vol. 97-98, pp. 693–696, 2001.

[24] C.-K. Lin, Y. Ren, K. Amine, Y. Qin, and Z. Chen, "In situ high-energy X-ray diffraction to study overcharge abuse of 18650-size lithium-ion battery," *Journal of Power Sources*, vol. 230, pp. 32–37, 2013.

[25] H. F. Li, J. K. Gao, and S. L. Zhang, "Effect of overdischarge on swelling and recharge performance of lithium ion cells," *Chinese Journal of Chemistry*, vol. 26, no. 9, pp. 1585–1588, 2008.

[26] L. Zhang, Y. Ma, X. Cheng et al., "Capacity fading mechanism during long-term cycling of over-discharged $LiCoO_2$/mesocarbon microbeads battery," *Journal of Power Sources*, vol. 293, pp. 1006–1015, 2015.

[27] J. Shu, M. Shui, D. Xu, D. Wang, Y. Ren, and S. Gao, "A comparative study of overdischarge behaviors of cathode materials for lithium-ion batteries," *Journal of Solid State Electrochemistry*, vol. 16, no. 2, pp. 819–824, 2012.

[28] Y. Zheng, X. Han, L. Lu, J. Li, and M. Ouyang, "Lithium ion battery pack power fade fault identification based on Shannon entropy in electric vehicles," *Journal of Power Sources*, vol. 223, pp. 136–146, 2013.

[29] P. Taheri, S. Hsieh, and M. Bahrami, "Investigating electrical contact resistance losses in lithium-ion battery assemblies for hybrid and electric vehicles," *Journal of Power Sources*, vol. 196, no. 15, pp. 6525–6533, 2011.

[30] D. H. Doughty, *Vehicle battery safety roadmap guidance*, National Renewable Energy Lab.(NREL), Golden, CO (United States), 2012.

[31] D. Ouyang, M. Chen, Q. Huang, J. Weng, Z. Wang, and J. Wang, "A review on the thermal hazards of the lithium-ion battery and the corresponding countermeasures," *Applied Sciences*, vol. 9, no. 12, p. 2483, 2019.

[32] B. Mao, C. Zhao, H. Chen, Q. Wang, and J. Sun, "Experimental and modeling analysis of jet flow and fire dynamics of 18650-type lithium-ion battery," *Applied Energy*, vol. 281, article 116054, 2021.

[33] A. W. Golubkov, D. Fuchs, J. Wagner et al., "Thermal-runaway experiments on consumer Li-ion batteries with metal-oxide and olivin-type cathodes," *RSC Advances*, vol. 4, no. 7, pp. 3633–3642, 2014.

[34] Y. Fernandes, A. Bry, and S. De Persis, "Identification and quantification of gases emitted during abuse tests by overcharge of a commercial Li-ion battery," *Journal of Power Sources*, vol. 389, pp. 106–119, 2018.

[35] Y. Chen, N. Liu, Y. Jie et al., "Toxicity identification and evolution mechanism of thermolysis-driven gas emissions from cathodes of spent lithium-ion batteries," *ACS Sustainable Chemistry & Engineering*, vol. 7, no. 22, pp. 18228–18235, 2019.

[36] Y. Zhang, H. Wang, W. Li, and C. Li, "Quantitative identification of emissions from abused prismatic Ni-rich lithium-ion batteries," *ETransportation*, vol. 2, article 100031, 2019.

[37] Y. Zhang, H. Wang, W. Li, C. Li, and M. Ouyang, "Size distribution and elemental composition of vent particles from abused prismatic Ni-rich automotive lithium-ion batteries," *Journal of Energy Storage*, vol. 26, article 100991, 2019.

[38] M. Henriksen, K. Vaagsaether, J. Lundberg, S. Forseth, and D. Bjerketvedt, "Laminar burning velocity of gases vented from failed Li-ion batteries," *Journal of Power Sources*, vol. 506, article 230141, 2021.

[39] D. Kong, G. Wang, P. Ping, and J. Wen, "A coupled conjugate heat transfer and CFD model for the thermal runaway evolution and jet fire of 18650 lithium-ion battery under thermal abuse," *ETransportation*, vol. 12, article 100157, 2022.

[40] H. J. Curran, "Developing detailed chemical kinetic mechanisms for fuel combustion," *Proceedings of the Combustion Institute*, vol. 37, no. 1, pp. 57–81, 2019.

[41] D. Kim, J. Shin, J. Kim, J. Park, Y. Son, and S. Park, "Effects of spray pattern and piston shape on in-cylinder flow in a two-cylinder spray-guided gasoline direct-injection optical

engine," *Applied Thermal Engineering*, vol. 234, article 121272, 2023.

[42] D. Kim and S. Park, "Spray characteristics of fouled gasoline direct injectors under flash boiling and sub-zero temperature conditions," *Case Studies in Thermal Engineering*, vol. 37, article 102259, 2022.

[43] D. Kim, J. Shin, Y. Son, and S. Park, "Characteristics of in-cylinder flow and mixture formation in a high-pressure spray-guided gasoline direct-injection optically accessible engine using PIV measurements and CFD," *Energy Conversion and Management*, vol. 248, article 114819, 2021.

[44] Z. Jia, Z. Huang, H. Zhai et al., "Experimental investigation on thermal runaway propagation of 18,650 lithium-ion battery modules with two cathode materials at low pressure," *Energy*, vol. 251, article 123925, 2022.

[45] J. Fang, J. Cai, and X. He, "Experimental study on the vertical thermal runaway propagation in cylindrical lithium-ion batteries: effects of spacing and state of charge," *Applied Thermal Engineering*, vol. 197, article 117399, 2021.

[46] L. Zhang, Q. Duan, J. Xu, X. Meng, J. Sun, and Q. Wang, "Experimental investigation on suppression of thermal runaway propagation of lithium-ion battery by intermittent spray," *Journal of Energy Storage*, vol. 58, article 106434, 2023.

[47] X. Liu, D. Xu, X. Meng et al., "Thermal runaway suppression effect of water mist on 18650-cylinder lithium-ion batteries with different cathode materials," *Case Studies in Thermal Engineering*, vol. 35, article 102155, 2022.

[48] J. Xu, Q. Duan, L. Zhang, Y. Liu, J. Sun, and Q. Wang, "The enhanced cooling effect of water mist with additives on inhibiting lithium ion battery thermal runaway," *Journal of Loss Prevention in the Process Industries*, vol. 77, article 104784, 2022.

[49] S. Chen, Z. Wang, and J. Liu, "A semi-quantitative analysis of infrared characteristics of thermal runaway ejection behaviour of lithium-ion battery," *Journal of Energy Storage*, vol. 71, article 108166, 2023.

[50] R. Tschirschwitz, C. Bernardy, P. Wagner et al., "Harmful effects of lithium-ion battery thermal runaway: scale-up tests from cell to second-life modules," *RSC Advances*, vol. 13, no. 30, pp. 20761–20779, 2023.

[51] D. P. Finegan, M. Scheel, J. B. Robinson et al., "*In-operando* high-speed tomography of lithium-ion batteries during thermal runaway," *Nature Communications*, vol. 6, no. 1, p. 6924, 2015.

[52] G. Wang, D. Kong, P. Ping et al., "Revealing particle venting of lithium-ion batteries during thermal runaway: a multi-scale model toward multiphase process," *ETransportation*, vol. 16, article 100237, 2023.

[53] A. García, J. Monsalve-Serrano, R. L. Sari, and S. Martinez-Boggio, "An optical investigation of thermal runaway phenomenon under thermal abuse conditions," *Energy Conversion and Management*, vol. 246, article 114663, 2021.

[54] A. García, J. Monsalve-Serrano, R. L. Sari, and S. Martinez-Boggio, "Influence of environmental conditions in the battery thermal runaway process of different chemistries: thermodynamic and optical assessment," *International Journal of Heat and Mass Transfer*, vol. 184, article 122381, 2022.

[55] A. García, P. Zhao, J. Monsalve-Serrano, D. Villalta, and S. Martinez-Boggio, "Optical diagnostics of the venting spray and combustion behaviour during Li-ion battery thermal runaway induced by ramp heating," *Applied Thermal Engineering*, vol. 218, article 119308, 2023.

[56] R. D. Keane and R. J. Adrian, "Optimization of particle image velocimeters. I. Double pulsed systems," *Measurement Science and Technology*, vol. 1, no. 11, p. 1202, 1990.

[57] E. Stamhuis and W. Thielicke, "PIVlab–towards user-friendly, affordable and accurate digital particle image velocimetry in MATLAB," *Journal of Open Research Software*, vol. 2, p. 30, 2014.

[58] I. Watanabe and J.-i. Yamaki, "Thermalgravimetry-mass spectrometry studies on the thermal stability of graphite anodes with electrolyte in lithium-ion battery," *Journal of Power Sources*, vol. 153, no. 2, pp. 402–404, 2006.

[59] G.-H. Kim, A. Pesaran, and R. Spotnitz, "A three-dimensional thermal abuse model for lithium-ion cells," *Journal of Power Sources*, vol. 170, no. 2, pp. 476–489, 2007.

[60] Q. Wang, P. Ping, X. Zhao, G. Chu, J. Sun, and C. Chen, "Thermal runaway caused fire and explosion of lithium ion battery," *Journal of Power Sources*, vol. 208, pp. 210–224, 2012.

[61] D. Wang, L. Zheng, X. Li et al., "Effect of high Ni on battery thermal safety," *International Journal of Energy Research*, vol. 44, no. 14, pp. 12158–12168, 2020.

[62] G. Wei, R. Huang, G. Zhang et al., "A comprehensive insight into the thermal runaway issues in the view of lithium-ion battery intrinsic safety performance and venting gas explosion hazards," *Applied Energy*, vol. 349, article 121651, 2023.

[63] L. Yuan, T. Dubaniewicz, I. Zlochower, R. Thomas, and N. Rayyan, "Experimental study on thermal runaway and vented gases of lithium-ion cells," *Process Safety and Environmental Protection*, vol. 144, pp. 186–192, 2020.

[64] H. Lee, M. Yanilmaz, O. Toprakci, K. Fu, and X. Zhang, "A review of recent developments in membrane separators for rechargeable lithium-ion batteries," *Energy & Environmental Science*, vol. 7, no. 12, pp. 3857–3886, 2014.

[65] Y. Sun, D. Ren, G. Liu et al., "Correlation between thermal stabilities of nickel-rich cathode materials and battery thermal runaway," *International Journal of Energy Research*, vol. 45, no. 15, pp. 20867–20877, 2021.

[66] H. Konishi, T. Yuasa, and M. Yoshikawa, "Thermal stability of $Li_{1-y}Ni_xMn_{(1-x)/2}Co_{(1-x)/2}O_2$ layer-structured cathode materials used in Li-ion batteries," *Journal of Power Sources*, vol. 196, no. 16, pp. 6884–6888, 2011.

[67] Y. Wang, H. Wang, Y. Zhang et al., "Thermal oxidation characteristics for smoke particles from an abused prismatic Li (Ni0. 6Co0. 2Mn0. 2) O2 battery," *Journal of Energy Storage*, vol. 39, article 102639, 2021.